

High-Density Intracortical Microelectrode Arrays With Multiple Metallization Layers for Fine-Resolution Neuromonitoring and Neurostimulation

S. R. I. Gabran, *Member, IEEE*, Muhammad Tariqus Salam, *Member, IEEE*, Joshua Dian, Youssef El-Hayek, J. L. Perez Velazquez, Roman Genov, *Senior Member, IEEE*, Peter L. Carlen, M. M. A. Salama, *Fellow, IEEE*, and Raafat R. Mansour, *Fellow, IEEE*

Abstract—Intracortical microelectrodes play a prominent role in the operation of neural interfacing systems. They provide an interface for recording neural activities and modulating their behavior through electric stimulation. The performance of such systems is thus directly meliorated by advances in electrode technology. We present a new architecture for intracortical electrodes designed to increase the number of recording/stimulation channels for a given set of shank dimensions. The architecture was implemented on silicon using microfabrication process and fabricated 3-mm-long electrode shanks with six relatively large ($110\ \mu\text{m} \times 110\ \mu\text{m}$) pads in each shank for electrographic signal recording to detect important precursors with potential clinical relevance and electrical stimulation to correct neural behavior with low-power dissipation in an implantable device. Moreover, an electrode mechanical design was developed to increase its stiffness and reduce shank deflection to improve spatial accuracy during an electrode implantation. Furthermore, the pads were post-processed using pulsed low current electroplating and reduced their impedances by ~ 30 times compared to the traditionally fabricated pads. The paper also presents microfabrication process, electrodes characterization, comparison to the commercial equivalents, and *in vitro* and *in vivo* validations.

Index Terms—Functional electric stimulation (FES), intracortical electrodes, microelectrode arrays, neural interfacing.

I. INTRODUCTION

FUNCTIONAL electric stimulation (FES) is a neuromodulation technique developed for stimulating peripheral nerves [1], the spinal cord [2], or the brain in order to regulate

the activity of a cluster of neurons [3]. It has the potential to provide invaluable medical procedures and therapies for the diagnosis and treatment of central nervous system disorders and to enable the development of neuron interfaces for medical prostheses [4]–[9]. FES offers methods for restoring motor function and regulating organ activities through direct interaction with the nervous system in order to activate nerves that innervate extremities and organs [10]. Intracortical electrodes designed for chronic recording and stimulation are key elements in neuromodulation and functional electric stimulation systems [11]–[14]. Electrode design influences the reliability and efficacy of electrotherapeutic techniques, and advancements in electrode technology will meliorate the quality of the therapy delivered.

Progress in intracortical electrode design has been marked by many innovations, beginning with glass micropipettes limited to single-site recording and suitable for *in vitro* and single-cell recording [15]. Microwire bundle electrodes then replaced glass micropipettes for rodent and primate signal-recording procedures with an increase in the number of recording spots to four (tetropdes) or nine (niotropdes) [16]. Such electrodes are easy to fabricate; however, they have low positional accuracy and are limited to a single channel per wire [17]. Electrode design benefited greatly from advances in microfabrication technology, and thin-film electrodes were introduced in 1970 [18]. Thin-film technology employed microfabrication and photolithographic techniques to produce multisite electrodes for recording [19] and stimulation applications [20]. Multi-shank electrodes expanded the number of channels that could be incorporated and enabled the creation of multidimensional electrode arrays with high spatial resolution. Increasing the number of channels improves the functionality of the electrode. A dense constellation of interface channels would thus enhance the spatial accuracy and mapping resolution of the interface, allow superior current steering, and provide redundant channels in order to compensate for post-implantation pad malfunctions.

Increasing the number of channels per shank is limited by the dimensions of the pads and the electrode. Microelectrode recording pads normally have small surface areas ($176\ \mu\text{m}^2$ to $703\ \mu\text{m}^2$) [21] for spike recordings [22] and multiunit recordings [23], while local field potential (LFP) recording requires a minimum area of $11\ 304\ \mu\text{m}^2$ [24]. The LFP is

Manuscript received November 04, 2012; revised April 09, 2013 and July 15, 2013; accepted August 01, 2013. Date of publication October 07, 2013; date of current version November 04, 2013.

S. R. I. Gabran is with the Department of Electrical and Computer Engineering, University of Waterloo and Center for Integrated RF Engineering (CIRFE Lab), Waterloo, ON, N2L 3G1 Canada.

M. T. Salam and R. Genov are with the Department of Electrical and Computer Engineering, University of Toronto, Toronto, ON, M5S 3G4 Canada.

J. Dian, Y. El-Hayek, and P. L. Carlen are with the Toronto Western Research Institute, Epilepsy Program, University Health Network, University of Toronto, Toronto, ON, M5G 2M9 Canada.

J. L. Perez Velazquez is with the Neurosciences and Mental Health Research Institute, Hospital for Sick Children, Toronto, ON, M5G 1X8 Canada.

M. M. A. Salama and R. R. Mansour are with the Department of Electrical and Computer Engineering, University of Waterloo, Waterloo, ON, N2L 3G1 Canada.

Color versions of one or more of the figures in this paper are available online at <http://ieeexplore.ieee.org>.

Digital Object Identifier 10.1109/TNSRE.2013.2279403

comprised of slow voltage waves (<100 Hz) that result from neural activity. These low-frequency spectral contents are considered electrographic signal precursors with potential clinical relevance [25]. However, electrodes with smaller surfaces may block or degrade LFP recordings, yielding higher impedance in low-frequency bandwidths. An additional factor is that neural stimulation requires relatively large electrode pads, but larger pads and high-count stimulation channels necessitate expanded electrode dimensions. Also, the interconnect pads and connectors contribute to the electrode dimensions. The result would be an increase in tissue trauma and the associated foreign body response, and eventually, the glial scar would form around the electrodes which would inhibit its effective operation [26]. Stimulation pads are usually designed to have large areas ($\sim 12\,000\ \mu\text{m}^2$) for the delivery of sufficient electric charges to suppress abnormal electrographic seizure [27], [28]. Expanding the pad area also reduces channel impedance, a desirable characteristic of LFP recordings and implanted electrical stimulation devices because it extends battery life.

In this paper, the microelectrode architecture and the associated fabrication process are developed to address the design and fabrication challenges of multi-channel stimulation and LFP recording electrodes. The microelectrodes were fabricated in densely packed channels for LFP recording and stimulation applications. The electrode architecture was designed to exploit a given set of shank and pad dimensions and allows increasing the number of stimulation channels without changing the shank width to reduce tissue trauma and maintain the biocompatibility of the electrode. The electrode was designed to have rigid structure in order to avoid mechanical deflection and improve insertion spatial accuracy. Furthermore, low impedance in each channel was achieved by increasing the pad area and utilizing pad postprocessing technique described later. This paper also explains the mechanical and electrical modeling and analysis of the electrode, describes the fabrication of the prototypes, and presents a postprocessing technique for reducing electrode impedance. The electrical characterization and impedance measurements are elaborately discussed, as well as *in vitro* stimulation on human brain slice and *in vivo* recordings from adult rats are illustrated.

II. ELECTRODE DESIGN AND LAYOUT

The metal layer of the electrode is comprised of a number of elements including: interface pads that come into contact with the neurons, interconnect pads for mating the electrode to the external circuitry, and routing tracks that couple the interface pads with the associated interconnect terminals. In conventional electrode designs, the interface pads and routing tracks are accommodated on the same metallization layer. Fig. 1 illustrates sketches for the conventional (a) and proposed (b) electrode layouts, the shown diagrams demonstrate arbitrary shank thicknesses which will be discussed quantitatively in the mechanical design analysis in Section III. The tracks are considered overhead that consume the limited shank area, and adding more channels requires expanding the shank width. This would aggravate tissue trauma and intensify the associated foreign body response. Using narrow tracks would reduce the shank width; however, the minimum track width is

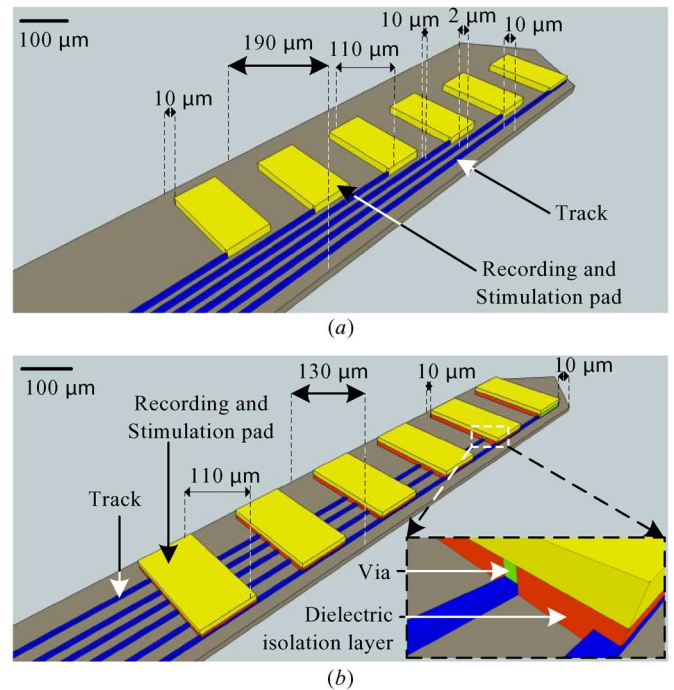


Fig. 1. Comparison of a conventional electrode (a) and the proposed double metallization layer architecture (b). Conventional design accommodates the stimulation pads (yellow) and tracks (blue) on the same metal layer. The proposed architecture separates the pads and tracks into two distinct metal layers, and the associated pads and tracks are connected through buried vias (red).

bound by the resolution associated with the microfabrication process. Narrow tracks would also contribute to the electrode impedance. Moreover, reducing track width might aggravate its mechanical vulnerability when used in flexible electrode structures. In conclusion, narrow tracks offer limited improvement to channel packing; and the maximum number of pads is constrained by the shank width.

The proposed electrode architecture is comprised of two metallization layers separated by dielectric film. The bottom layer forms the routing tracks, while the top carries the exposed interconnect and stimulation pads. The associated pads and tracks are connected through the dielectric layer by means of buried vias. A previously implemented commercial recording electrode involved layering the routing tracks underneath the pads [21]. However, the electrode architecture presented and the associated fabrication process were developed for electrodes that accommodate a large number of low-impedance stimulation channels, with the stimulation pads being characterized by surface areas up to 120 times larger than the recording pads [27]. Such large areas significantly lower channel impedance and can thus extend battery life for implantable devices. The new architecture utilizes the vertical space in order to increase channel packing, while reducing the width of the shank to the pad dimensions.

Fig. 1 provides a comparison of conventional layouts and the one proposed, illustrating the difference in shank width required for packing six pads on the conventional shank ($190\ \mu\text{m}$) and the proposed shank ($130\ \mu\text{m}$). In Fig. 1, the top view of the electrode shank shows the stimulation pads (yellow) overlapping with the tracks (red) and isolated by the dielectric layer

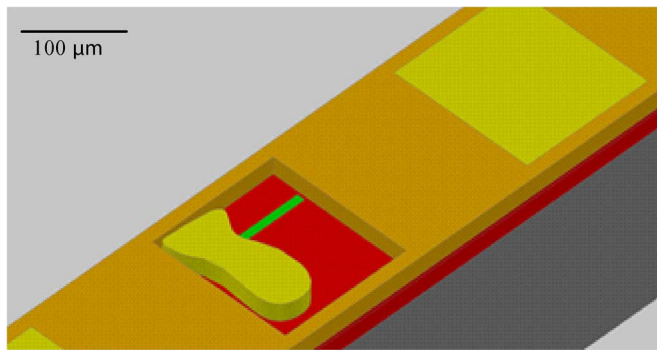


Fig. 2. Sectional view of the proposed stimulation electrode; the figure reveals portion of the stimulation pad (yellow), buried via (green), dielectric isolation layer (red), and passivation layer (orange).

in which the buried vias (green) were created in order to connect the pairs of pads. The sectional view in Fig. 2 illustrates the anatomy of the electrode: a portion of a stimulation pad is shown in contact with the associated track through the via, and the top surface of the electrode is passivated with a dielectric layer.

III. ELECTRODE MODELING AND DESIGN OPTIMIZATION

The geometry of the electrode and the design of the metallization layer were optimized in order to improve mechanical and electric performances. The electrode structure was designed so that it would survive implantation and postoperative mechanical loads. The nonuniform structure of metal layers was modeled to investigate the parameters contributing to the electrode electric resistance which is required to be reduced in order to reduce power consumption during current-controlled stimulation. Finite element parametric modeling and analysis were conducted using Ansys Workbench 12, and sensitivity analysis was employed to investigate the effects of different design parameters on electrode performance.

A. Mechanical Analysis

The electrode was designed to have a stiff structure in order to reduce mechanical deflection during the surgical procedure and also to improve the accuracy of spatial implantation into the deep brain of rats or mice, e.g., in the hypothalamus, nucleus accumbens, or brainstem regions. Silicon was chosen for the structural layer because it provides the required mechanical properties and is suitable for microfabrication. Although silicon is considered brittle, miniaturizing the structure to micro-dimensions reduces the probability of defects and critical cracks so that the properties of the material can reach the defect-free theoretical limit and the fracture strength of the structure is enhanced. Silicon was therefore used to fabricate a thin probe with shank thickness of $10\ \mu\text{m}$. The thin shank exhibited flexible structure that could be bent to angles exceeding 90° [16]. However, to maintain the stiffness essential to maintain the spatial accuracy of implanting the silicon probe; a brittle silicon model was employed in the mechanical analysis for bulk structures.

To minimize tissue trauma, the layout of the electrode was developed so that brain tissue could be penetrated without insertion devices, i.e., insertion stylus. The styli or similar

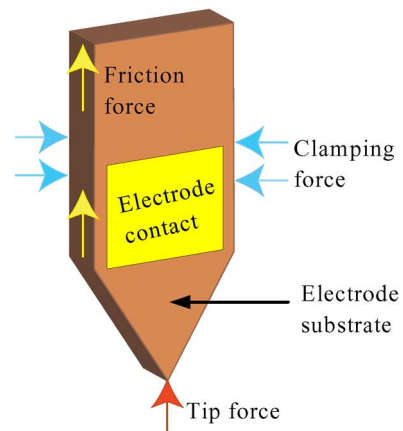


Fig. 3. Free body diagram illustrating the forces acting on the shank during insertion.

insertion equipment increases the electrode footprint leading to aggravated tissue damage. The design therefore incorporates the structural rigidity required for withstanding the mechanical loads inherent in insertion and operation. Reducing the footprint of the electrode reduces tissue trauma and enhances biocompatibility [30], [31] but also compromises structural strength and mechanical performance. During brain tissue penetration, the electrode is subjected to buckling and fracture failures [32]. While during operation, it experiences mechanical loading caused by the cortical dislocation that occurs due to the pulsating forces generated by the circulatory and respiratory systems and by the rotational acceleration of the head [33]. The insertion force applied to the electrode should be sufficient to overcome the axial reaction force created during tissue penetration. The latter force is caused by the superposition of the tip, with clamping and friction forces acting on the electrode side walls and the tip, as illustrated in the free body diagram shown in Fig. 3. The penetration force was estimated in the literature to be $1\ \text{mN}$ [34], [35], and this value was therefore assumed for the electrode modeling.

B. Buckling Analysis

Buckling is a failure mode that vulnerates slender structures and disturbs the structural equilibrium when the exerted axial force exceeds a threshold value identified as the critical load. This process drives the electrode into an unstable state and causes its eventual collapse. The critical point during electrode insertion occurs immediately prior to tissue penetration, when the axial load and the effective length of the electrode reach their peaks [36]. The critical load value is a function of the geometry, material, and end support configuration of the electrode. The buckling resistance drops with the presence of material defects; geometrical asymmetry; and eccentric loading, which introduce bending moments and promote curvature. To prevent buckling failure, the electrode should be designed to have a critical load greater than the force required for tissue penetration. During tip penetration through tissue, the electrode base is held by a stereotaxic micro-manipulator apparatus which restricts the electrode displacement along the direction of penetration. This condition is called fixed-pinned loading. However, due to electrode flexibility; the accuracy of

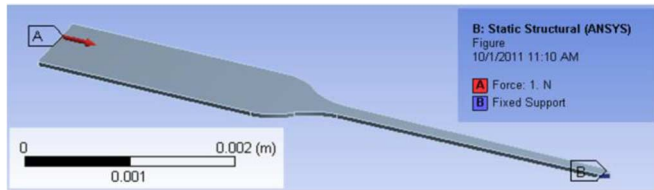


Fig. 4. Fixed-free Eigen buckling model for the electrode layout.

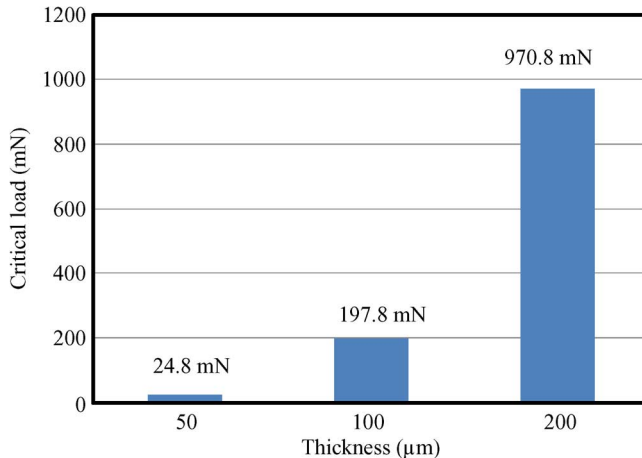


Fig. 5. Histogram of critical loads for different electrode layouts: Fixed-free Eigen buckling analysis.

the spatial implantation was sometimes compromised when thin silicon substrate or polyimide-based flexible probes were used. As a result, the electrode was designed to have stiff structure and a safety factor of 10 was applied in order to ensure the strength, straightness, and stiffness of the silicon probes [33]. The electrode was modeled for Eigen buckling analysis, and unity axial force was applied to its base. Different layouts were modeled and analyzed, and the critical loads were estimated to represent the forces that can provoke buckling failure for different electrode designs and thicknesses. Shanks with uniform cross-sections were modeled in order to calibrate the simulator using analytical techniques. A parametric model was created for the optimization of the design, and the shank width was fixed at 130 μm, with a thickness varying from 20 to 200 μm. The complete design model is shown in Fig. 4 and critical loads for select 3-mm-long electrode thicknesses are demonstrated in Fig. 5. The results of the analysis show that a 3 mm shank with a thickness of 20 μm has a critical load of 5 mN, which drops to 0.9 mN for a 6 mm shank. A safety factor of 10 that corresponds to 10 mN was applied to find thickness of the shank [33].

C. Lateral Bending Stress Analysis

During implantation and operation, the electrode is affected by lateral forces normal to the shank, which induce bending moments and create out-of-plane deformation that can cause fractures in brittle structures. Fixed-free support condition that represents loading according to the worst case scenario was assumed, and two sets of analyses were executed. The first was an extension of the buckling analysis in order to estimate the maximum principal stresses in response to compressive axial loading. This study was followed by a static structural analysis,

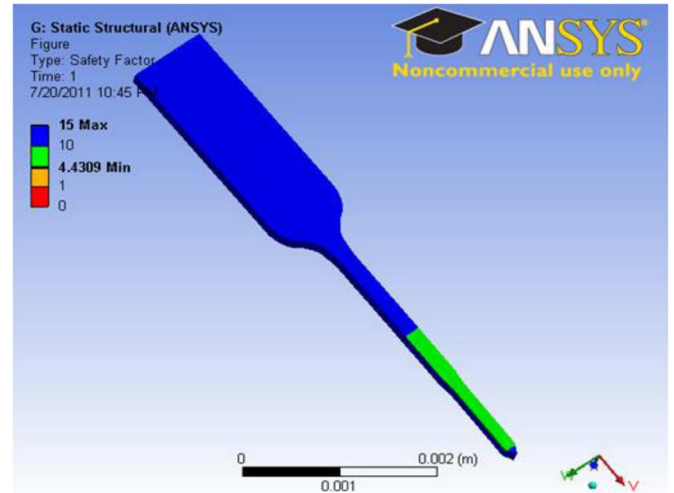


Fig. 6. Safety factor distribution for lateral bending loading of 200 μm silicon electrode.

in which the electrode was loaded with a 1 mN lateral bending force equivalent to the value of the force required for electrode insertion. When a brittle silicon beam is subjected to mechanical stress, it undergoes minor elastic deformation followed by a sudden fracture as the stress exceeds the yield strength; therefore, the fracture analysis of the brittle structures included consideration of the maximum principal stress theory (Rankine criterion), based on the assumption of the ultimate tensile strength (UTS) being the maximum loading limit. The safety factor was calculated based on a comparison of the failure load with the design load according to (1), and a value equal to or greater than 10 was considered acceptable. To identify high stress spots, safety factor distribution contours were plotted in order to indicate the ratio between the maximum stress and the maximum strength for the different models, and the electrode layout was modified so that points of concentrated stress would be avoided. *Stress Safety Factor*

$$\text{Stress Safety Factor} = \frac{\text{Failure Stress}}{\text{Design Stress}} = \frac{\sigma_y}{\sigma_1} \quad (1)$$

where the failure load (σ_y) is the yield stress, and the design load (σ_1) is the allowable stress.

Lateral bending forces applied to the shank of the electrode created tensile stresses on one side and compressive stresses along the other. Consequently, the side subjected to the compressive stresses does not fail because the ultimate compressive strength for a brittle material is greater than the tensile strength. Through stress analysis, the principal stress exerted on the shank in response to the applied forces was estimated, and the results implied that the minimum thickness at which the silicon electrode could achieve a safety factor of 10 throughout its structure was 200 μm, as shown in Fig. 6. The results of the mechanical analyses were thus considered to be design guidelines for preventing mechanical failure.

The complete single-shank electrode layout was extended to create a quad-shank array that provides 2-D constellation of interfacing channels with 1 mm shank spacing. The array was modeled in order to investigate its response to lateral bending loading. Lateral force of 10 mN was applied normal to the base

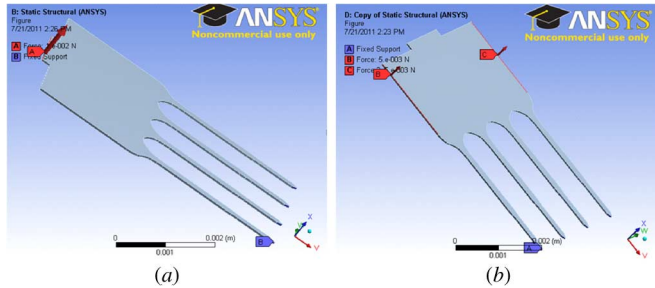


Fig. 7. Lateral loading of quad-shank electrode array: (a) force is applied to base edge and (b) force is divided equally and applied to base sides.

TABLE I
PARAMETRIC MODEL VARIABLES

Model parameter	Minimum	Maximum
Routing track length	1000 μm	6000 μm
Routing track width	1 μm	10 μm
Routing track thickness	300 nm	1 μm
Pad via width	2 μm	30 μm
Pad via length	50 μm	100 μm
Pad via thickness	50 μm	100 μm
Temperature (discrete)	20°C	37°C

of the electrode, and the shank tips were fixed, in accordance with the assumption of fixed-free support conditions. As shown in Fig. 7, the forces were loaded in two different configurations: the first was applied to the top edge of the base, and the second was divided into two equal components applied to each of the sides of the base. The results show a slight drop in the resistance of the array to lateral bending failure, so in order to achieve the required safety factor; the minimum thickness was increased to 250 μm . The electrode was also subject to lower stresses when the force was applied at the sides of the base than when it was applied to its tip, findings that suggest that the sides of the electrode base should be supported during penetration.

D. Electrical Analysis

The electrode architecture contains two metal layers comprised of several components: routing tracks, stimulation pads, interconnect pads, and buried vias. The hypothesis was that components with narrow cross-sections, e.g., the routing tracks and the vias at the stimulation pads, would be the predominant contributors to the impedance of the metal structure. A finite element model was created in order to estimate the dc resistance of the metallization layers and to explore the effects of different electrode components on its value. The ac impedance was experimentally characterized, as described in Section V-A.

A unity voltage was applied at the stimulation pad, and the interconnect pad was grounded. The current through the metallic structure was estimated, and the resistance was calculated. The modeling produced a resistance of 70.94 Ω , a simulated result in good agreement with the experimentally measured resistance discussed elaborately in Section V-A. The results obtained from the postprocessing and parametric model sensitivity analyses were helpful for the investigation of the effects of different variables and parameters on the electrode resistance. The dimensions of the components were varied within a range of prac-

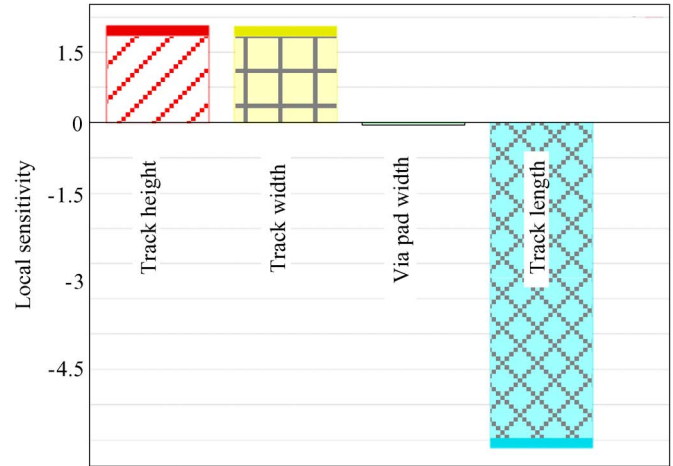


Fig. 8. Postprocessing results of the parametric model: sensitivity analysis exhibiting the influence of electrode dimensions on the current flow. Based on the components dimensions, track length dominates the contribution to the track dc impedance, while its cross section has moderate effect.

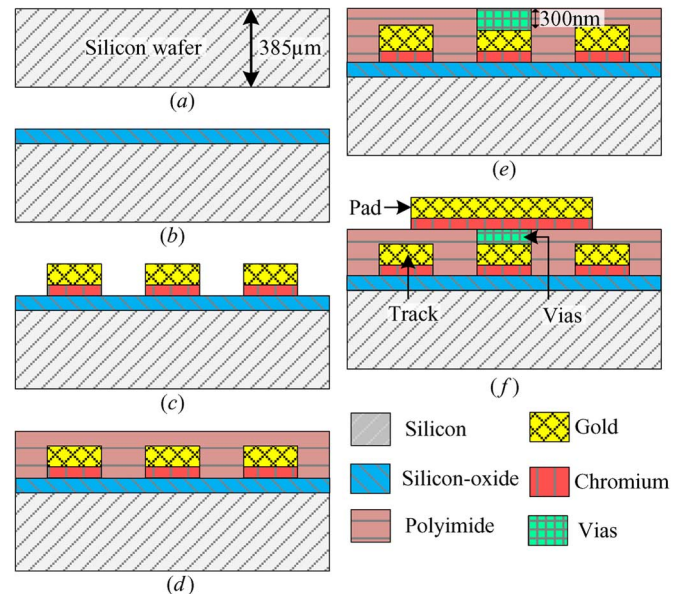


Fig. 9. Electrode fabrication process: Starting with clean silicon wafer (a), an oxide layer is deposited (b), then the first metallization layer was formed and patterned (c) followed by spin coating and curing the polyimide dielectric layer (d). The polyimide layer was patterned, dry etched, and coated with metallic layer to create the buried vias (e). The second metallization layer was deposited and patterned to create the pads (f), and finally the electrode was released.

tical fabrication values, and two operation temperatures were configured to represent ambient lab (20 °C) and human body (37 °C) conditions. The values of the parametric model are listed in Table I. The results of the sensitivity analysis were plotted as shown in Fig. 8, and the lengths of the bars indicate the relative contribution of each component to the dc resistance. Based on the given of constraints and boundaries for the components dimensions; the sensitivity analysis exhibited the dominance of the track length to the dc impedance value, whereas the cross section of the track and the width vias have only moderate effects, and the other parameters appear to have a negligible influence. A thermoelectric model was created as a means of investigating the joule heating and the resultant rise in temperature caused by the current flow. The simulation, executed

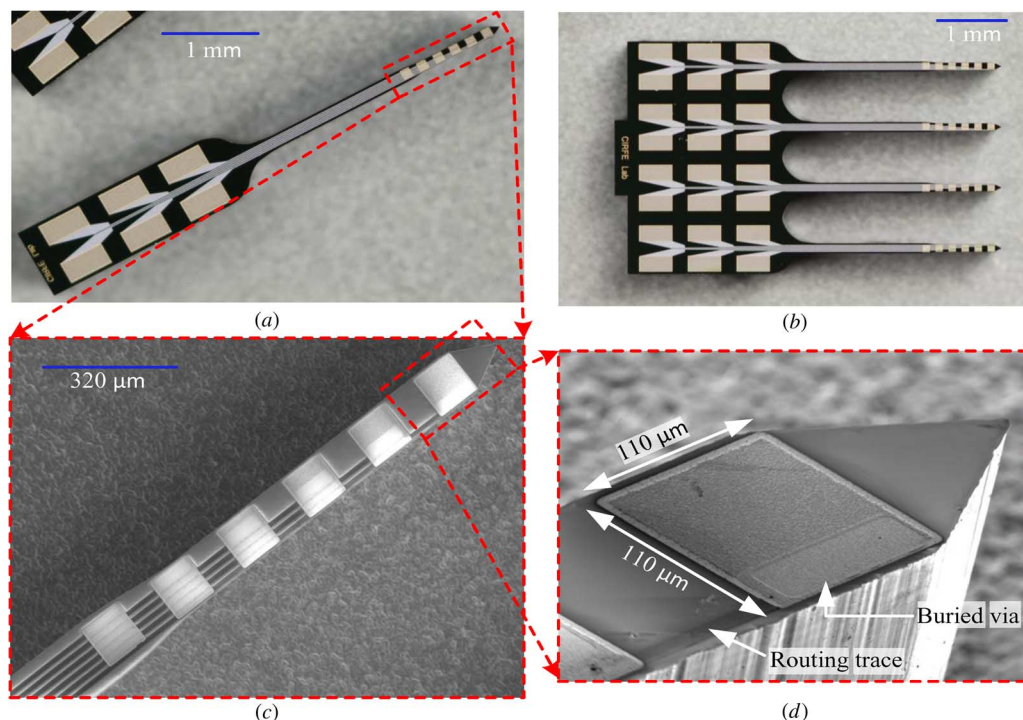


Fig. 10. Fabricated electrodes. (a) Single shank electrode with six gold stimulation pad. (b) Quad shank electrode with six gold stimulation pads per shank providing 2-D array of stimulation channels. (c) SEM picture of the electrode shank. (d) Close up view for the electrode tip.

at 20 °C and 37 °C, revealed a temperature rise of less than 1 °C, which is within the allowable limit [37]. The results of the parametric model and sensitivity analysis demonstrate that track length is the most dominant factor in dc impedance and joule heating. Based on these findings, the thickness of the metal layer and cross-sectional area of the track can be chosen so that reliable mechanical performance and satisfactory adhesion to other layers in the structure of the electrode are ensured.

IV. ELECTRODE FABRICATION

Several materials were investigated with respect to their suitability for use in the electrode components, including the structural, metallization, insulation, and passivation layers. Silicon, which is appropriate for multilayer microfabrication, was chosen as the structural layer. Single- and quad-shank electrodes were implemented on a 385 μm silicon wafer, with the shanks designed to be 3 mm long and 130 μm wide. Each shank accommodated six 110 μm × 110 μm pads, and the tracks were 10 μm in width. The fabrication process is outlined in Fig. 9. To prevent short-circuiting the adjacent tracks due to the low wafer resistance, the wafer was RCA cleaned and passivated with PECVD silicon oxide. The oxide layer was deposited to a thickness of 300 nm using the following process parameters: pressure: 900 mTorr, temperature: 250 °C, RF power: 60 W, gas flow rate: silane: 5 sccm, N₂: 118 sccm, N₂O: 140 sccm, and deposition was run for 300 s. The first metallization layer was formed of chromium (200 nm) and gold (300 nm) deposited using e-beam evaporation and dc sputtering deposition standard recipes for Intlvac Nanochrome Deposition System. The second dielectric layer was made of 1.2 μm of polyimide PI-2562. Polyimide precursor was spin coated at 5000 RPM and cured using standard polyimide recipe to a maximum temperature of

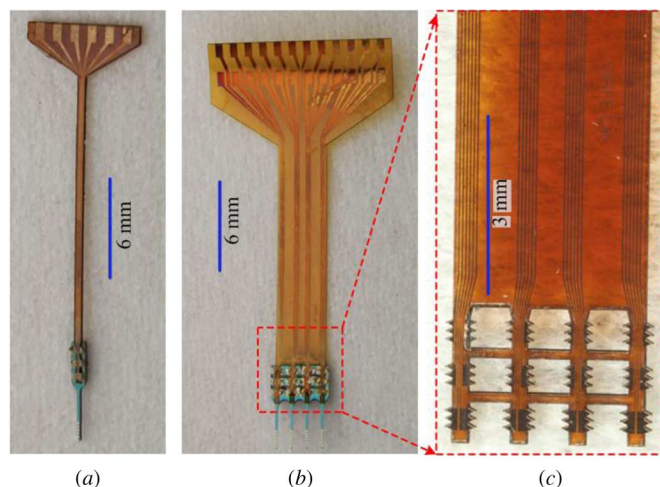


Fig. 11. Electrode assembly. (a) Single shank electrode with six gold stimulation pads. (b) Quad shank electrode with six gold stimulation pads per shank providing 2-D array of stimulation channels. (c) Flexible interconnect cable tips.

300 °C. The buried vias were patterned and dry etched using oxygen plasma in Trion RIE Phantom RIE system using the following process parameters: pressure: 250 mTorr, ICP: 100 W, RIE: 50 W, O₂: 30 sccm for 400 s. The second metallization layer was formed of chromium (200 nm) and gold (800 nm) and was patterned to create the exposed interface and interconnect pads. Gold was sputtered to achieve reliable via coverage and to provide a biocompatible tissue contact with chromium as the adhesion layer for the gold. The final step involved the patterning of the contour of the electrode with an aluminum hard mask (500 nm) and its release by means of a standard Bosch deep reactive ion etching process.

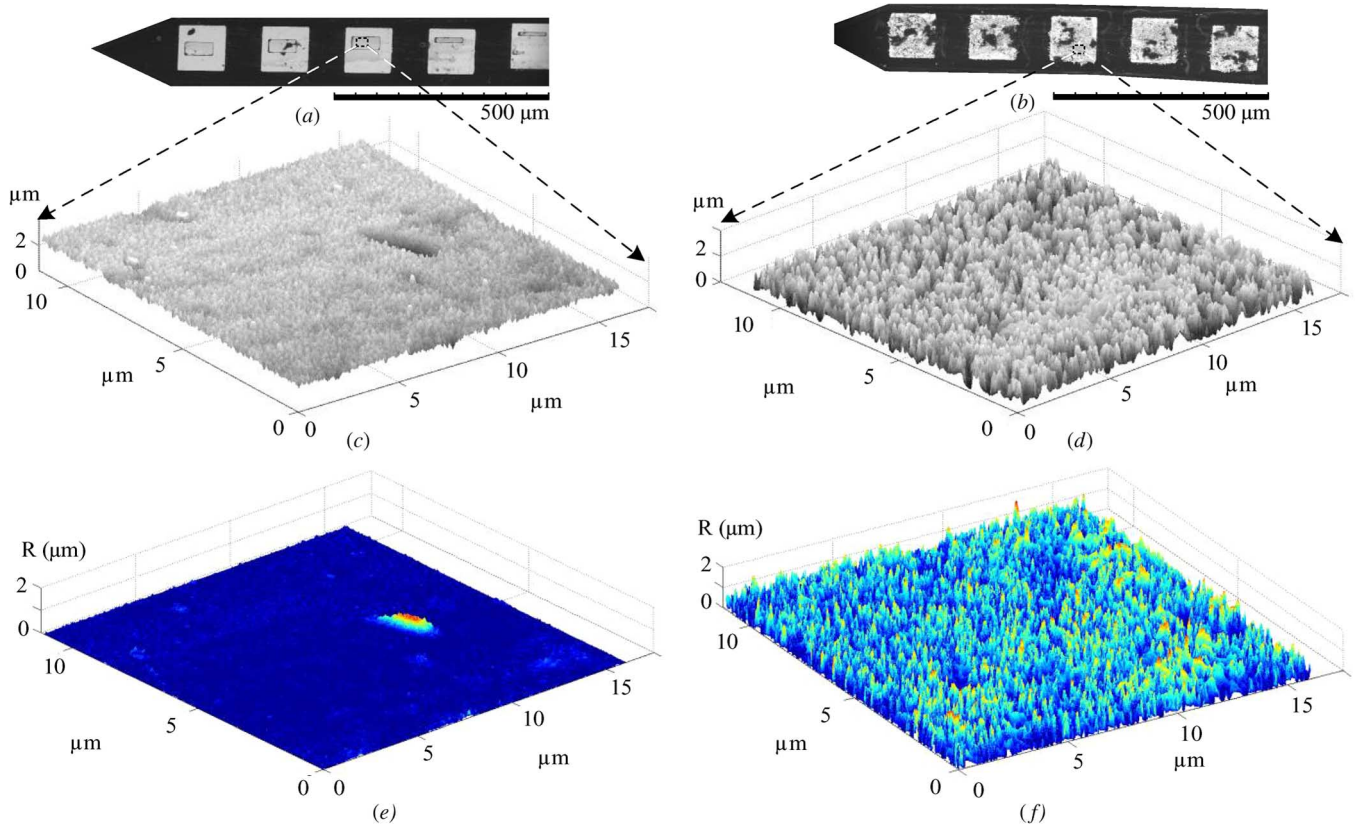


Fig. 12. Scanning electron microscope images of (a) SME and (b) NME, 3-D views of surface morphology of SME in (c) and NME in (d), and roughness of SME in (e) and NME in (f).

The single- and quad-shank electrodes are depicted in Fig. 10(a) and (b), and the electrode shank and its attributes are illustrated in the photograph of the scanning electron microscope (SEM) provided in Fig. 10(c). A close-up of the electrode tip is shown in Fig. 10(d), with the routing track, buried via, and stimulation pad for one of the channels indicated.

The electrode was coupled to external circuitry using custom-designed flexible interconnect cables fabricated on a 50 μm polyimide substrate. Multiple layers (copper–titanium–chromium: 1500 nm – 150 nm – 150 nm) were deposited and patterned to form the tracks and pads. The surface was passivated with a second layer of polyimide and patterned using an aluminum hard mask (300 nm) and oxygen plasma to expose the pads. The final step was the etching of the mask and the release of the cable using laser micromachining [38]. The cable was then attached to the electrode with a conductive silver epoxy. The final assembly is shown in Fig. 11(a) and (b). As depicted in Fig. 11(c), the cable tip was designed to have triangular pads in order to enhance the conductive epoxy bonding of the electrode pads to the electrode channels.

The implemented electrodes surface profiles were visually inspected in high-resolution SEM images and quantified corresponding 3-D profile data using Atomic Force Microscope (Agilent Technologies, Inc.). The smooth and rough surfaces were initially differentiated visually from the high-resolution SEM images. Later, root mean square (rms) values were quantified from the 3D profile data. The RMS value below 300 nm visually represents smooth surface in SEM images; however, above the 300 nm value visually represents rough surface.

The fabricated smooth-surface microelectrodes (SME) demonstrated higher electrode impedance; thus, pad surface modification technique was developed using low-current pulsed electroplating process. The resulting nanotextured electrodes (NME) exhibited rough surface and lower impedance. Fig. 12(a) and (b) presents SEM images of smooth surface electrodes and the postprocessing rough surface electrodes. The 3D profile data illustrate the electrodes surface profiles in Fig. 12(c) and (d). The roughness (R) of the surface in Fig. 12(c) and (d) is measured using following:

$$R(i, j) = |x(i, j) - \bar{x}| \quad (2)$$

where $x(i, j)$ is the normalized individual height value of the surface and \bar{x} the mean value of all the height data points. The number of measurement points is $N \times m$, where $i = 1, 2, 3 \dots N$ and $j = 1, 2, 3 \dots m$. The rms roughness (R_q) is calculated from the standard deviation of the height data according to (3) [39]. R_q describes the deviation of the measurement points to the centerline and this way describes the variability of the measured profile from centerline [40]

$$R_q = \frac{1}{N} \left(\sum_{i=1}^N \frac{1}{M} \left(\sum_{j=1}^M (x(i, j) - \bar{x})^2 \right) \right). \quad (3)$$

R_q of the SME and NME are 128 and 562 nm, respectively.

V. RESULTS

The fabricated microelectrodes were characterized electrically, and later, the microelectrodes were validated *in vitro*

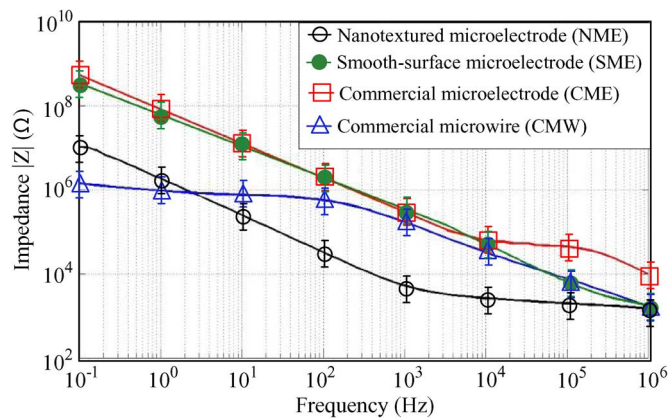


Fig. 13. FRA of electrode–electrolyte interface: Pad impedance magnitude.

experiment for their effectiveness with respect to human brain slice stimulation and *in vivo* experiment for EEG recordings performance from an adult rat. Details of the measurements and validations were described below.

A. Electrode Characterization

The electrical properties of the electrode were characterized by measuring the dc resistance of the channels and estimating the ac electrode–tissue interface impedance. The dc channel resistance was measured using a two-wire microprobe station, a controlled voltage source, and a digital multimeter. The I - V characteristics were plotted, and the resistance was calculated to be 72Ω , a result in good agreement with the simulated resistance value (70.94Ω).

The electrode–tissue interface impedance was estimated using frequency response analysis (FRA) and electrochemical impedance spectroscopy (EIS). A two-electrode standard electrochemical cell was set up using a 0.9% sodium-chloride saline solution, a platinum counter electrode, a Solatron SI 1287 Electrochemical Interface, and a Solatron SI 1260 Impedance/Gain-Phase Analyzer. To obtain impedance measurements, a 10 mV signal was swept from 1 MHz to 0.1 Hz, and the current was recorded. The measurements were repeated for different pads on the test electrodes. A commercial microelectrode (CME) (Neuronexus: part # A \times 16 – 5 mm-150-703)) and microwire (CMW) (PlasticsOne: part # MS303/1-B/SP). The resulting average impedance values recorded were 2160 k Ω and 424 K Ω at 100 Hz, respectively.

Stimulation using high impedance electrodes required an increase in the driving current, which is not appropriate for battery-powered implants. Accordingly, it was necessary to reduce the electrode impedance and this was achieved through expanding the electrode–electrolyte interface area. A low-cost postprocessing technique using pulsed low current electroplating was developed to deposit rough thin film of gold on the electrode pads. This technique increased the pad surface area resulting in a significant drop in the interface impedance to an average of 68 k Ω at 100 Hz, a level lower than that achieved with the commercial twisted wire electrode (MS301-1/B, PlasticsOne Inc., Roanoke, VA, USA). The impedance magnitude for the normal (SME) and postprocessed (NME) pads as well as CME and CMW are illustrated in Fig. 13, and the values at 100 Hz are listed in Table II. Table III compares the presented

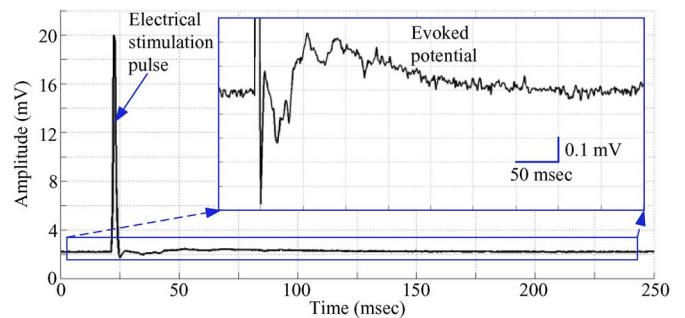


Fig. 14. *In vitro* validation: Captured signals exhibiting stimulation pulse and evoked potential.

TABLE II
FRA OF THE ELECTRODE–ELECTROLYTE INTERFACE IMPEDANCE

Electrode Characteristics	Impedance at 100 Hz	
	Magnitude	Phase
CME ^a	2160 ± 0.05 k Ω	-77.6°
CMW ^b	424 ± 10 k Ω	-58.6°
SME ^c pad	2272 ± 0.05 k Ω	-67.9°
NME ^d pad	68.66 ± 1 k Ω	-81.4°
CME differential channel	4830 ± 0.05 k Ω	-72.3°
CMW differential channel	575 ± 13 k Ω	-27.1°
SME differential channel	5590 ± 0.1 K Ω	-65.7°
NME differential channel	179 ± 4 k Ω	-82.7°

^aCME: commercial microwire, ^bCME: commercial microelectrode, ^cSME: Smooth-surface microelectrodes, ^dNME: Nanotextured microelectrodes

TABLE III
COMPARISON WITH THE COMMERCIAL ELECTRODES

Characteristic	Commercial microelectrode (CME) [21]	Commercial microwire (CMW) [41]	This works
Electrode area	177 μm^2	12000 μm^2	12100 μm^2
Roughness	0.12 μm	0.15 μm	0.562 μm
Theoretical thermal noise	7.8 μVrms	3.2 μVrms	0.9 μVrms
Noise contribution	8.3 μVrms	4.1 μVrms	1.2 μVrms
Average impedance (1 to 100Hz)	101 M Ω	1.5 M Ω	500 k Ω

electrode with other commercial microelectrode [21] and microwire [41]. The pads on the CME have small areas and smooth surfaces, and exhibited high channel impedance which failed to deliver a charge that suffices electrical stimulation from the implantable device. Although these electrodes can successfully detect neural spikes, they degrade the mean field potential power in theta (4–7 Hz), alpha (8–13 Hz), beta (13–30 Hz), and gamma (30–100 Hz) frequency bands [29]. On the other hand, a SME has a relatively wide smooth-surface electrode pad area but also exhibits comparatively higher noise. The electrode used in this work has a wide rough-surface electrode pad, which yields the lowest impedance and best noise level.

B. In Vitro Validation

The *in vitro* experiment was performed with ethics committee approval in the Krembil Neuroscience Centre Research,

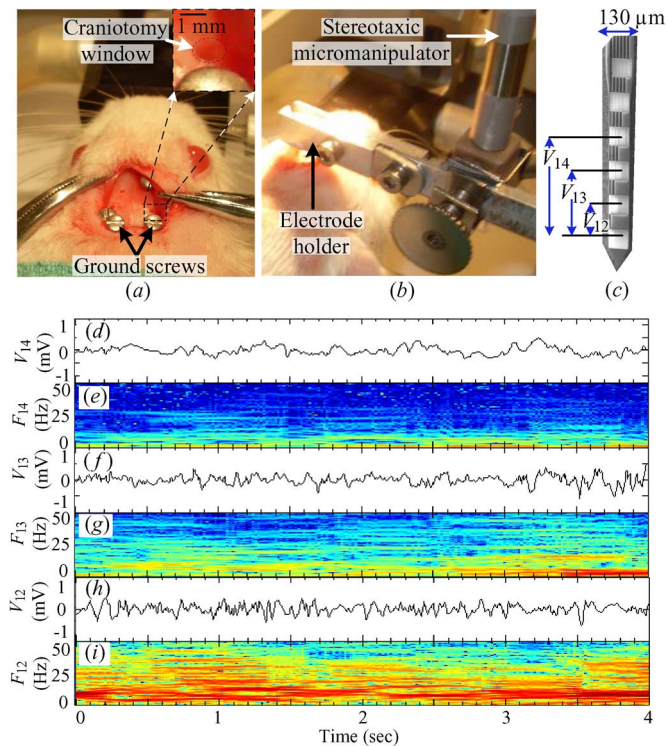


Fig. 15. *In vivo* validation: (a) rat's craniotomy under general anesthesia, (b) microelectrode implantation for EEG recordings, (c) microelectrode configuration for the bipolar recordings, (d) is neural signal recording V_{14} in between $500 \mu\text{m}$ tissue, (e) is frequency analysis of V_{14} , (f) is neural signal recording V_{13} in between $300 \mu\text{m}$ tissue, (g) is frequency analysis of V_{13} , (h) is neural signal recording V_{12} in between $100 \mu\text{m}$ tissue, and (i) is frequency analysis of V_{12} .

Toronto Western Hospital. The electrode was set up for the *in vitro* stimulation of a human hippocampus brain tissue sample obtained on the same day from a resective epilepsy surgery patient. During testing, the tissue sample was secured in place using a vacuum stage, with a stream of oxygenated (95%) artificial cerebrospinal fluid (ACSF) sustaining its viability. Carbon-dioxide (5%) was bubbled through the solution in order to buffer the bicarbonates in the ACSF. This tissue sample was stimulated using a voltage-controlled current stimulator. A 0.1 mA stimulation current pulse was generated, and the charge was delivered to the tissue sample. Also a standard concentric recording probe was used for monitoring and recording the electric activities generated from the tissue. The stimulation pulse and successive evoked potential were recorded, and the experiment was repeated six times in order to confirm the results. The signals captured from the individual experiments were averaged and plotted, as shown in Fig. 15. The captured signal demonstrates the stimulation pulse followed by the evoked potential as a response to the successful stimulation of the hippocampus.

C. *In Vivo* Validation

The microelectrodes were validated for neural signal recording by means of an acute *in vivo* experiment that was conducted at the Neurosciences and Mental Health Research Institute, Hospital for Sick Children, Toronto. A wistar rat ($\sim 250 \text{ gm}$) underwent craniotomy with general anesthesia [Fig. 15(a)], and the microelectrodes were implanted through

the somatosensory area into the hippocampus [Fig. 15(b)]. Following the implantation, neural signals were recorded bipolarly at a 200 Hz sampling rate. Fig. 15(c) shows the implanted microelectrode configuration for the recordings, and Fig. 15(d)–(i) illustrate the signals recorded at a variety of distances between tissues, along with their corresponding signal frequency plots. Recordings V_{14} and V_{13} captured neural activities from tissues between $500 \mu\text{m}$ and $300 \mu\text{m}$, respectively. On the other hand, Fig. 15(h) depicts the similar bipolar neural signal (V_{12}) recorded from $100 \mu\text{m}$ tissue, highlighting the high frequency sharp waves [Fig. 15(h)]. Because of the wider regions recorded in V_{14} and V_{13} , the signal frequencies F_{14} and F_{13} shown in Fig. 15(e) and (g) are relatively lower than the F_{12} frequency indicated in Fig. 15(i). The proposed microelectrode array is thus capable of recording specific regional neural activity as well as the local field potential.

VI. CONCLUSION

This research has introduced a novel intracortical microelectrode architecture developed as a means of exploiting the available electrode area in order to maximize the number of recording or stimulation channels accommodated per shank without expanding the width of the shank. This architecture enables the channel packing per electrode to be increased without a corresponding expansion of the footprint. The electrode design was implemented for the creation of a rigid intra-cortical array electrode to reduce mechanical deflection during insertion and improve implantation spatial accuracy.

Mechanical and electrical finite element models were developed, and sensitivity analyses and correlation matrices revealed the influence on performance of varying the design parameters of the electrode. The layout of the electrode was optimized in order to minimize its footprint while maintaining the required mechanical strength. The electrode was also modeled with the goal of optimizing the metal layer design and minimizing the dc channel resistance. Silicon was chosen for the implementation of the electrode, and both the implementation and the fabrication process were explained. The coupling of the electrodes to the circuits was achieved through the design and fabrication of flexible interconnects cables. A low-cost postprocessing technique for reducing the electrode–tissue interface impedance was developed and resulted in the successful dropping of the channel impedance from an average value of $2270 \text{ k}\Omega$ to $70 \text{ k}\Omega$ at 100 Hz. The experimental results of the characterization of the electrode have been provided for both *in vitro* and *in vivo* testing

ACKNOWLEDGMENT

The infrastructure used for this work would not have been possible without the significant contributions of the Natural Sciences and Engineering Research Council of Canada, Ontario Brain Institute, the Canada Foundation for Innovation, the Ontario Ministry of Research and Innovation, and Industry Canada.

REFERENCES

- [1] F. Hanai, "Effect of electrical stimulation of peripheral nerves on neuropathic pain," *Spine*, vol. 25, no. 5, pp. 1886–1892, 2000.
- [2] C. L. Sadowsky, "Electrical stimulation in spinal cord injury," *NeuroRehabilitation*, vol. 16, no. 3, pp. 165–169, 2001.

- [3] S. Acharya, H. L. Benz, M. Mollazadeh, N. E. Crone, and N. V. Thakor, "Toward electrocorticographic control of a dexterous upper limb prosthesis: Building brain-machine interfaces," *IEEE Pulse*, vol. 3, pp. 38–42, 2012.
- [4] T. A. Fofonoff, S. M. Martel, N. G. Hatsopoulos, J. P. Donoghue, and I. W. Hunter, "Microelectrode array fabrication by electrical discharge machining and chemical etching," *IEEE Trans. Biomed. Eng.*, vol. 51, no. 6, pp. 890–895, Jun. 2004.
- [5] D. Higgins and G. Banker, *Primary Dissociated Cell Cultures. In Culturing Nerve Cells*. Cambridge, MA: MIT Press, 1998, pp. 37–78.
- [6] A. Schwartz, "Cortical neural prosthesis," *Annu. Rev. Neurosci.*, vol. 27, pp. 453–485, 2004.
- [7] D. J. DiLorenzo and J. D. Bronzino, *Neuroengineering*. Boca Raton, FL: CRC Press, 2007.
- [8] G. Santhanam, S. I. Ryu, B. M. Yu, A. Afshar, and K. V. Shenoy, "A high performance neurally-controlled cursor positioning system," in *Proc. 2nd Int. IEEE EMBS Conf. Neural Eng.*, 2005, pp. 494–500.
- [9] W. R. Patterson, Y. Song, C. W. Bull, I. Ozden, A. P. Deangelis, C. Lay, J. L. McKay, A. V. Nurmikko, J. D. Donoghue, and B. W. Connors, "A microelectrode-microelectronic hybrid device for brain implantable neuroprosthesis applications," *IEEE Trans. Biomed. Eng.*, vol. 51, no. 10, pp. 1845–1853, Oct. 2004.
- [10] S. C. Schachter, J. Gutttag, S. J. Schiff, and D. L. Schomer, Summit Contributors, "Advances in the application of technology to epilepsy: The CIMIT/NIO epilepsy innovation summit," *Epilepsy Behav.*, vol. 16, pp. 3–46, 2009.
- [11] T. L. Skarpaas and M. J. Morrell, "Intracranial stimulation therapy for epilepsy," *Neurotherapeutics*, vol. 6, no. 2, pp. 238–243, 2009.
- [12] R. Fisher, V. Salanova, T. Witt, R. Worth, T. Henry, R. Gross, K. Oommen, and I. Osorio *et al.*, "Electrical stimulation of the anterior nucleus of thalamus for treatment of refractory epilepsy," *Epilepsia*, vol. 51, no. 5, pp. 899–908, 2010.
- [13] I. Osorio, M. G. Frei, S. Sunderam, J. Giftakis, N. C. Bhavaraju, S. F. Schaffner, and S. B. Wilkinson, "Automated seizure abatement in humans using electrical stimulation," *Ann. Neurol.*, vol. 57, no. 2, pp. 258–268, 2005.
- [14] M. T. Salam, F. Mounaim, D. K. Nguyen, and M. Sawan, "A low-power miniaturized seizure detector with responsive neurostimulation for the treatment of refractory epilepsy," *J. Low Power Electron.*, vol. 8, no. 2, 2012.
- [15] K. Kagoo, *Microelectrode Arrays for Neural Recording School Eng., UCSC*, 2005.
- [16] K. Najafi, J. Ji, and K. D. Wise, "Scaling limitations of silicon multi-channel recording probes," *IEEE Trans Biomed Eng.*, vol. 37, no. 1, pp. 1–11, Jan. 1990.
- [17] W. He and R. V. Bellamkonda, "A molecular perspective on understanding and modulating the performance of chronic Central Nervous System (CNS) recording electrodes," in *Source Indwelling Neural Implants: Strategies for Contending With the In Vivo Environment*, W. M. Reichert, Ed. Boca Raton, FL: CRC Press, 2008, ch. 6.
- [18] K. D. Wise, J. B. Angell, and A. Starr, "An integrated-circuit approach to extracellular microelectrodes," *IEEE Trans. Biomed. Eng.*, vol. 17, no. 3, pp. 238–247, Jul. 1970.
- [19] I. H. Stevenson and K. P. Kording, "How advances in neural recording affect data analysis," *Nature Neurosci.*, vol. 14, pp. 139–142, 2011.
- [20] R. Shulyzki, K. Abdelhalim, A. Bagheri, C. Florez, P. Carlen, and R. Genov, "256-site active neural probe and 64-channel responsive cortical stimulator," in *Proc. IEEE Custom Integrat. Circuits Conf.*, Sep. 2011, pp. 1–4.
- [21] NeuroNexus, *Electrode Arrays* [Online]. Available: <http://www.neuronexus.com>
- [22] G. Schneider and D. Nikolić, "Detection and assessment of near-zero delays in neuronal spiking activity," *J. Neurosci. Methods*, vol. 152, no. 1–2, pp. 97–106, 2006.
- [23] T. J. Blanche, M. A. Spacek, J. F. Hetke, and N. V. Swindale, "Polytrodes: High-density silicon electrode arrays for large-scale multiunit recording," *J. Neurophysiol.*, vol. 93, no. 5, pp. 2987–3000, 2005.
- [24] D. Xing, C. Yeh, and R. M. Shapley, "Spatial spread of the local field potential and its laminar variation in visual cortex," *J. Neurosci.*, vol. 29, no. 37, pp. 11540–11549, 2009.
- [25] J. L. Perez Velazquez, L. G. Dominguez, V. Nenadovic, and R. A. Wennberg, "Experimental observation of increased fluctuations in an order parameter before epochs of extended brain synchronization," *J. Biol. Phys.*, vol. 37, pp. 141–152, 2011.
- [26] A. K. Koivuniemi, S. J. Wilks, A. J. Woolley, and K. J. Otto, "Multimodal, longitudinal assessment of intracortical microstimulation," *Progress Brain Res.*, vol. 194, pp. 131–144, 2011.
- [27] P. Rajdev, M. Ward, and P. Irazoqui, "Effect of stimulus parameters in the treatment of seizures by electrical stimulation in the kainate animal model," *Int. J. Neural Syst.*, vol. 21, no. 2, pp. 151–162, Apr. 2011.
- [28] R. E. Hampson, T. D. Coate, G. A. Gerhardt, and S. A. Deadwyler, "Ceramic-based microelectrode neuronal recordings in the rat and monkey," *Proc. IEEE Eng. Med. Biol. Soc.*, pp. 3700–3703, Sep. 2003.
- [29] A. Bagheri, S. R. I. Gabran, M. T. Salam, J. L. Perez Velazquez, R. R. Mansour, M. M. A. Salama, and R. Genov, "1024-channel-scalable neuromonitoring and neurostimulation wireless microsystem with low-impedance flexible nanotextured microelectrodes," in *Proc. IEEE Biomed. Circuits Syst. Conf.*, 2012.
- [30] P. K. Campbell, K. F. Jones, R. J. Huber, K. W. Horch, and R. A. Normann, "Silicon-based, three-dimensional neural interface," *IEEE Trans. Biomed. Eng.*, vol. 38, no. 8, pp. 758–768, Aug. 1991.
- [31] T. Yi, L. Li, and C. J. Kim, "Microscale material testing of single crystalline silicon," *Sensors Actuators*, vol. 83, pp. 172–178, 2000.
- [32] P. T. McCarthy, M. P. Rao, and K. J. Otto, "Simultaneous recording of rat auditory cortex and thalamus via a titanium-based multi-nucleus, microelectrode array," *J. Neural Eng.*, vol. 8, no. 4, pp. 1–21, 2011.
- [33] M. Salcman and M. J. Bak, "A new chronic recording intra-cortical microelectrode," *Med. Biol. Eng. Comput.*, no. 1, p. 14, 1976.
- [34] T. Suzuki, K. Mabuchi, and S. Takeuchi, "A 3-D flexible parylene probe array for multichannel neural recording," *IEEE EMBS Conf. Neural Eng.*, pp. 154–156, Mar. 2003.
- [35] S. F. Cogan, "Neural stimulation and recording electrodes," *Annu. Rev. Biomed. Eng.*, vol. 10, pp. 275–309, 2008.
- [36] H. Kim and J. S. Colton, "Fabrication and analysis of plastic hypodermic needles," *J. Med. Eng. Technol.*, vol. 29, 2005.
- [37] R. P. Michelson, "Electrical stimulation of the human cochlea a preliminary report," *Arch. Otolaryngol., Head Neck Surg.*, vol. 93, pp. 317–323, 1971.
- [38] S. R. I. Gabran, R. R. Mansour, and M. M. A. Salama, "Maskless pattern transfer using 355 nm laser," *J. Opt. Lasers Eng.*, vol. 50, no. 5, pp. 710–716, 2012.
- [39] *Surface Texture*, ASME B-46.1-1995, 1995.
- [40] F. Podczeczek, *Factors Influencing Adhesion. In Book: Particle-Particle Adhesion in Pharmaceutical Powder Handling*. London, U.K.: Imperial College Press, 1997.
- [41] *PlasticsOne, Multi-channel electrode* [Online]. Available: <http://www.plastics1.com>



S. R. I. Gabran (M'98) received the B.Sc. degree in electrical engineering from Cairo University, Cairo, Egypt, in 2002, and the M.A.Sc. and Ph.D. degrees in electrical engineering from the University of Waterloo, Waterloo, ON, Canada, in 2006 and 2012, respectively.

Currently, he is the co-founder and Director of Novela Inc., and a researcher with the CIRFE Lab, University of Waterloo, Waterloo, ON, Canada. His interests include micro-fabrication, neuro-engineering, intra-cortical implants and BioMEMS.



Muhammad Tariq Salam received the the B.A.Sc. degree in electrical and electronics engineering from the Islamic University of Technology (IUT), Gazipur, Bangladesh, in 2003, the M.A.Sc degree in electrical and computer engineering from Concordia University, Montreal, QC, Canada, in 2007, and the Ph.D. degree in electrical engineering from Polytechnique Montréal, Montreal, QC, Canada, in 2012.

Currently, he is a Postdoctoral Fellow at the University of Toronto, where he works at Intelligent Sensory Microsystems Laboratory, Neurosciences and Mental Health institute of Hospital for Sick Children Hospital, and Neuroscience division of Toronto Western Hospital. His specific research interests are in the areas of biosensing, detection and stimulation microsystems; implantable biomedical microdevices for continuous health monitoring, cognitive brain research, mental disease diagnosis, treatment, and rehabilitations.



Joshua Dian received the B.A.Sc. degree in engineering science specializing in biomedical engineering and the M.A.Sc. degree in electrical engineering from the University of Toronto, Toronto, ON, Canada, where he is currently working toward the Ph.D. degree in electrical engineering focusing on the characterization and control of epileptic seizures *in vitro*.



Youssef El-Hayek received the Ph.D. degree from the Department of Physiology, University of Toronto, Toronto, ON, Canada.

Following that, he completed a postdoctoral fellowship with Dr. Peter Carlen at the University Health Network in Toronto, ON, Canada. During his time there, he investigated the neurophysiology of epilepsy, aging, stroke, and Alzheimer's disease.

Dr. El-Hayek is a recipient of the Alzheimer's Society of Canada Doctoral Training award and the Canadian Institutes of Health Research "Science to

Business" award.



J. L. Perez Velazquez was born in Zaragoza, Spain, and received the degree of "Licenciado" in chemistry (biochemistry, Universities of Zaragoza and Complutense of Madrid), and the Ph.D. degree, in 1992, from the Department of Molecular Physiology and Biophysics, Baylor College of Medicine, Houston, TX, USA, homologated to Doctorate in Chemistry by the Spanish Ministry of Culture, in 1997.

He is an Associate Scientist in the Neuroscience and Mental Programme and the Brain and Behavior Center at the Hospital For Sick Children in Toronto, and Associate Professor at the University of Toronto.



Roman Genov (S'96-M'02-SM'11) received the B.S. degree in electrical engineering from Rochester Institute of Technology, Rochester, NY, USA, in 1996, and the M.S.E. and Ph.D. degrees in electrical and computer engineering from The Johns Hopkins University, Baltimore, MD, USA, in 1998 and 2002, respectively.

He held engineering positions at Atmel Corporation, Columbia, MD, USA, in 1995 and Xerox Corporation, Rochester, NY, USA, in 1996. He was a visiting researcher in the Laboratory of Intelligent Systems, Swiss Federal Institute of Technology (EPFL), Lausanne, Switzerland, in 1998, and in the Center for Biological and Computational Learning, Massachusetts Institute of Technology, Cambridge, MA, USA, in 1999. He is presently an Associate Professor in the Department of Electrical and Computer Engineering at the University of Toronto, Toronto, ON, Canada. His research interests are primarily in the area of implantable, wearable, and disposable biomedical electronics. This includes analog and digital VLSI circuits, systems and algorithms for electrical, chemical and photonic sensory information acquisition and energy-efficient signal processing with various medical applications such as brain-silicon interfaces and DNA microarrays.

Dr. Genov is a co-recipient of Best Paper Award of IEEE Biomedical Circuits and Systems Conference, Best Student Paper Award of IEEE International Symposium on Circuits and Systems, Best Paper Award of IEEE Circuits and Systems Society Sensory Systems Technical Committee, Brian L. Barge Award for Excellence in Microsystems Integration, MEMSCAP Microsystems Design Award, DALSA Corporation Award for Excellence in Microsystems Innovation, and Canadian Institutes of Health Research Next Generation Award. He was a Technical Program co-Chair at IEEE Biomedical Circuits and Systems Conference.

He was an Associate Editor of IEEE TRANSACTIONS ON CIRCUITS AND SYSTEMS-II: EXPRESS BRIEFS and IEEE SIGNAL PROCESSING LETTERS.

Currently he is an Associate Editor of IEEE TRANSACTIONS ON BIOMEDICAL CIRCUITS AND SYSTEMS and serves on the Imagers, MEMS, Medical, and Displays Subcommittee of the *International Solid-State Circuits Conference*.



Peter L. Carlen is a Professor of Medicine (Neurology), Physiology, and Institute of Biomaterials and Biomedical Engineering at the University of Toronto. He is a clinician/scientist, specializing in epilepsy and neurodegenerative diseases at the Toronto Western Hospital of the University Health Network. He was formerly the Head of Neurology at the Addiction Research Foundation. In 1989, he was appointed Director of the Playfair Neuroscience Unit and Neuroscience Research at the University Health Network for a 10 year term, where he is now

a Senior Scientist and Head of the Division of Fundamental Neuroscience. He has over 250 peer-reviewed biomedical publications and six patents. His main research interests are mechanisms of neural synchrony and entrainment in the context of epilepsy, the fetal alcohol syndrome, hypoglycemic seizures, and neurodegenerative processes. He also is an active neurological clinician with a practice focused on patients with epilepsy.



M. M. A. Salama (F'02) received the B.Sc. and M.Sc. degrees in electrical engineering from Cairo University, Cairo, Egypt, in 1971 and 1973, respectively, and the Ph.D. degree in electrical engineering from the University of Waterloo, Waterloo, ON, Canada, in 1977.

Currently, he is a Professor in the Department of Electrical and Computer Engineering, University of Waterloo, Waterloo, ON, Canada. His interests include the operation and control of distribution systems, power-quality monitoring and mitigation, asset management, and electromagnetics. He has consulted widely with government agencies and the electrical industry.

Dr. Salama is a registered Professional Engineer in the Province of Ontario.



Raafat R. Mansour (S'84-M'86-SM'90-F'01) was born in Cairo, Egypt, on March 31, 1955. He received the B.Sc. (with honors) and M.Sc. degrees from Ain Shams University, Cairo, Egypt, in 1977 and 1981, respectively, and the Ph.D. degree from the University of Waterloo, Waterloo, ON, Canada, in 1986, all in electrical engineering.

In 1981, he was a Research Fellow with the Laboratoire d'Electromagnetisme, Institut National Polytechnique, Grenoble, France. From 1983 to 1986, he was a Research and Teaching Assistant with the Department of Electrical Engineering, University of Waterloo. In 1986, he joined COM DEV Ltd., Cambridge, ON, Canada, where he held several technical and management positions with the Corporate Research and Development Department. In 1998, he received the title of a Scientist. In January 2000, he joined the University of Waterloo, as a Professor with the Electrical and Computer Engineering Department. He holds a Natural Sciences and Engineering Research Council of Canada (NSERC) Industrial Research Chair in RF engineering with the University of Waterloo. He is the Founding Director of the Center for Integrated RF Engineering (CIRFE), University of Waterloo. He has authored or coauthored numerous publications in the areas of filters and multiplexers, high-temperature superconductivity and microelectromechanical systems (MEMS). He is a coauthor of "Microwave Filters for Communication Systems" (Wiley, 2007). He holds several patents related to areas of dielectric resonator filters, superconductivity and MEMS devices. His current research interests include MEMS technology and miniature tunable RF filters for wireless and satellite applications.

Dr. Mansour is a Fellow of the Engineering Institute of Canada (EIC) and a Fellow of the Canadian Academy of Engineering (CAE).